RESEARCH ARTICLE | OCTOBER 23 2024

Table-top laser-based terahertz high harmonic generation spectroscopy under magnetic fields and low temperatures



X. B. Wang ■ (a); H. Wang (b); J. Y. Yuan (b); X. Y. Zeng; L. Cheng (c); J. Qi (c); J. L. Luo (c); T. Dong (d); N. L. Wang (d)



Rev. Sci. Instrum. 95, 103007 (2024) https://doi.org/10.1063/5.0215129





Articles You May Be Interested In

Generation of terahertz pulses with arbitrary elliptical polarization

Appl. Phys. Lett. (November 2005)

Strong terahertz pulse induced Pockels and Kerr effect in crystalline quartz for ultrafast pulse switching

Appl. Phys. Lett. (July 2024)

FPGA-based measurements of the relative arrival time of a high-repetition rate, quasi-cw fourth generation light source

Rev. Sci. Instrum. (October 2024)





Table-top laser-based terahertz high harmonic generation spectroscopy under magnetic fields and low temperatures

Cite as: Rev. Sci. Instrum. 95, 103007 (2024); doi: 10.1063/5.0215129

Submitted: 22 April 2024 • Accepted: 8 October 2024 •

Published Online: 23 October 2024







AFFILIATIONS

- ¹ Beijing National Laboratory for Condensed Matter Physics, Institute of Physics, Chinese Academy of Sciences, Beijing 100190, China
- ²International Center for Quantum Materials, School of Physics, Peking University, Beijing 100871, China
- ³ State Key Laboratory of Electronic Thin Films and Integrated Devices, University of Electronic Science and Technology of China, Chengdu 610054, China
- a) Author to whom correspondence should be addressed: xinbowang@iphy.ac.cn
- ^{b)}Electronic mail: taodong@pku.edu.cn
- c) Electronic mail: nlwang@pku.edu.cn

ABSTRACT

We have developed a terahertz (THz) nonlinear spectrometer at low temperatures (1.5–300 K) and under high magnetic fields (up to 10 T) by combining the laser-driven table-top intense THz source with a superconducting magnet. The strong-field THz pump pulse was generated from LiNbO₃ crystal using the tilted-pulse-front technique and tightly focused into the center of the magnet by an off-axis parabolic mirror and a THz lens. The electric fields at the focus can achieve 500 kV/cm with a monocycle waveform and 30 kV/cm with a multicycle waveform at 0.5 THz. The sample was mounted on a low-temperature motorized rotation stage, which enables performing the polarization dependent measurements of the third harmonic generation (THG) intensity without rotating the incident THz pulses. The magnetic field direction can be rotated using a mechanical rotator, allowing for a convenient switch between Faraday and Voigt geometry. We demonstrate the excellent performance of our instrument by conducting THG measurements in the two-band superconductor MgB₂ as a function of temperature, sample azimuth angle, as well as in-plane and out-of-plane magnetic fields. The successful combination of the strong field THz source with magnetic fields enables us to study a variety of materials with magnetic-field-dependent properties of interest.

Published under an exclusive license by AIP Publishing. https://doi.org/10.1063/5.0215129

I. INTRODUCTION

The magnetic field is a clean knob for both probing and tuning symmetry-breaking phases and electronic topology in quantum materials. The magnetic field can have a substantial effect on quantum materials by, for example, inducing a change in the band structure of a metal or semimetal (e.g., the formation of Landau levels), driving a quantum phase transition, altering the ground states in frustrated magnets, revealing hidden orders, or inducing new phases in magnetic or charge ordered materials.

Following Landau's paradigm, the functional properties of quantum materials are mainly determined by the low-lying

elementary excitations. These excitations, including lattice vibrations (phonons), collective spin wave excitations in magnets (magnons), binding energy of electron-hole pairs (excitons), pairing energy gaps and Josephson plasmons in high-temperature superconductors, amplitude modes or phase modes in charge density wave compounds, etc., are exactly in the far-infrared or terahertz spectral range. In the last two decades, magneto-THz/infrared spectrometers have been developed to study the magnetic field dependence of the elementary excitations, as exemplified by the observation of exotic magnetic excitations in quantum magnets, 2–5 the quantized topological electromagnetic response in topological insulators, 6–8 and the Landau level transitions of Dirac electrons. 9,10 When one

extends the THz optical responses into the nonlinear response regime, combining access to applied magnetic fields with a strong field THz source provides an alternative knob for probing the functional properties of quantum materials in a nonlinear fashion and, more importantly, for manipulating the functionality of materials on demand. For instance, in the two-dimensional electron gas (2DEG) heterostructure, a sufficiently strong magnetic field forces the free electrons to form energy equidistant Landau levels, which are characterized by a cyclotron frequency. The two-dimensional coherent spectroscopy measurement with a 5 kV/cm electric field reveals a significant THz four- and six-wave mixing signature of the Landau level transitions beyond Kohn's theorem. This indicates the Landau level transitions may offer a unique playground for a quantum control with relatively low-field amplitudes. 11 The subsequent THz pump-THz probe magneto-optical measurement on monolayer graphene with non-equidistant Landau level transitions further observes the realization of strong light-matter coupling in Landauquantized graphene with the Rabi frequency exceeding the carrier wave frequency.¹² However, the reported table-top implementations have not been able to achieve stronger electric fields due to the long focus distance restricted by the magnets and the limitation of the generated THz power.

An alternative route to realize the magneto-THz nonlinear spectrometer is to couple the magnetic fields with the free electron laser (FEL) facilities, which can provide a sufficiently strong electric field THz pulse with tunability in a wide spectral range. The FELIX¹³ and ELBE^{14,15} facilities have successfully developed THz pump-probe spectrometers and THG spectroscopy under the magnetic field. 16 However, the limitations of the FEL facilities are rather obvious. First, the carrier envelope phase of FEL facilities except the TELBE FEL is not stable, which prevents subcycle resolved nonlinear response within the THz pulse. Second, the THz radiations from the FEL facilities are mostly multicycle. It is difficult to switch from the multicycle geometry to the monocycle configuration if one requires a comparison experiment. Finally, the available beamtime at the FEL facilities is very limited. Here, we have developed a terahertz high harmonic generation spectrometer based on table-top laser systems under magnetic fields. The electric fields inside the magnet center can achieve 500 kV/cm with a monocycle waveform and 30 kV/cm with a multicycle waveform at 0.5 THz. To test the

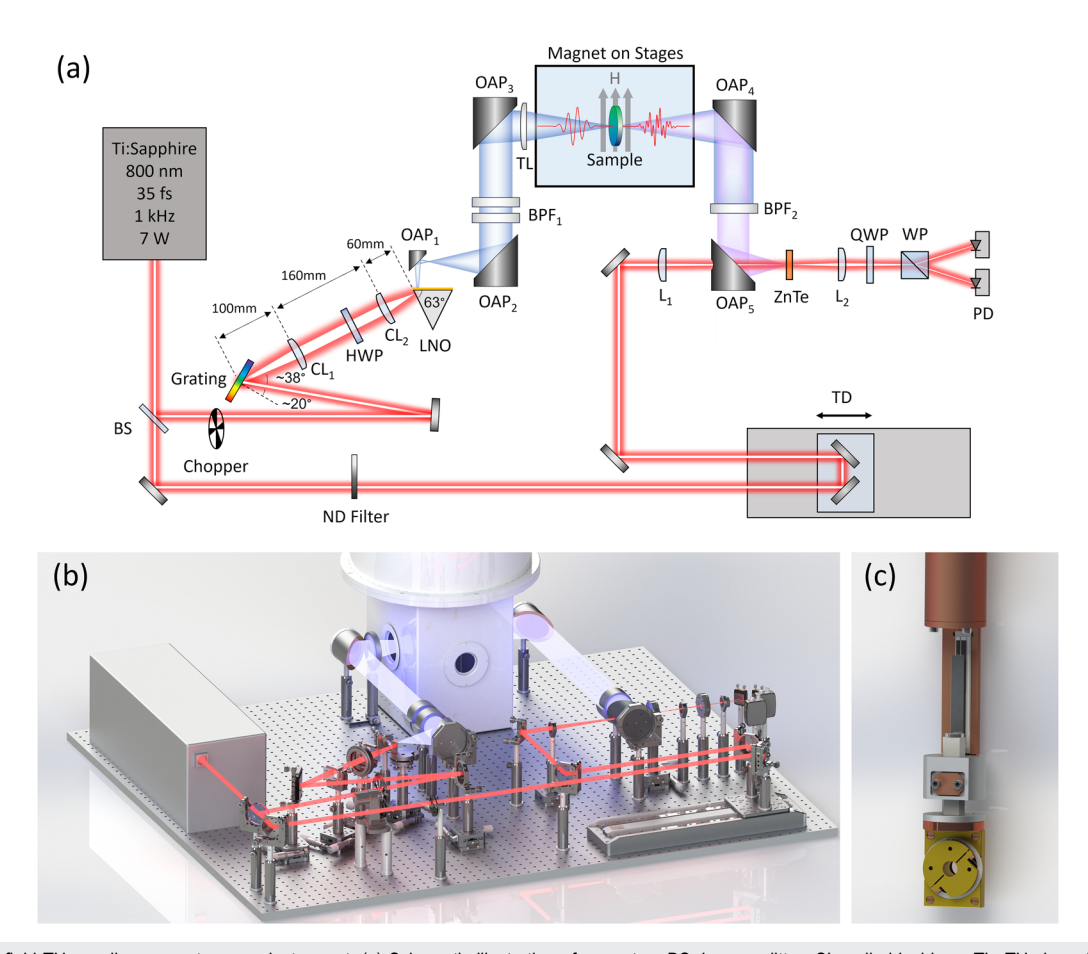


FIG. 1. Strong field THz nonlinear spectroscopy instrument. (a) Schematic illustration of our setup. BS: beam splitter; CL: cylindrical lens; TL: THz lens; L: focusing lens; HWP: half-wave plate; LNO: LiNbO₃; OAP: off-axis parabolic mirror; BPF: THz bandpass filter; QWP: quarter wave plate; WP: Wollaston prism; PD: photodiode; TD: time delay stage. (b) Experimental setup of the THz nonlinear spectrometer. (c) PZT-driven linear and rotation stages mounted at the end of the sample rod.

performance of our setup, we measured the THz THG of a typical two-band superconductor MgB_2 as a function of temperature, magnetic field, and sample azimuth angle. The excellent performance of our setup illustrates the versatile applicability of our spectrometer to a wide range of quantum materials, in which magnetic-field-induced exotic nonlinear response can be measured by the THz THG and even higher-order harmonic generation spectroscopy.

II. INSTRUMENT DESIGN

In Fig. 1, we show the schematic setup of our nonlinear THz spectroscopy instrument. It consists of two parts: (i) THz generation using the tilted-pump-pulse-front scheme and signal detection based on electro-optic (EO) sampling, and (ii) a 10 T split-pair superconducting magnet providing a cryogenic sample environment in the temperature range of 1.5–300 K. Both the THz generation and detection parts are placed outside the 50-G line of the superconducting magnet to minimize the magnetic force on the mechanical components. Below, we separately describe the two components of the instrument in detail.

A. Intense THz source

The intense monocycle THz pulses were generated by tiltedpump-pulse-front optical rectification 17,18 in a 5% MgO doped LiNbO₃ crystal (CTL Photonics) with a prism angle of 63°. We used an amplified Ti:Sapphire laser (Spectra Physics Spitfire ACE) with a pulse energy of 7 mJ, a pulse duration of 35 fs, a center wavelength of 800 nm, and a repetition rate of 1 kHz. The main laser beam was sent to a gold-coated blazed grating (Spectrogon) with a groove density of 1500 lines/mm. The efficiency of the diffraction at minus one order is greater than 90% for horizontal polarization. The incident and diffraction angles 18,19 were 20.4° and 58.2°, respectively. After the grating, the pump beam was collimated and focused onto the surface of LiNbO₃ by a 4f imaging telescope, consisting of two cylindrical lenses with 100 and 60 mm focal lengths, respectively. A half-wave plate was inserted between the two lenses to rotate the polarization of the diffracted beam from the horizontal to the vertical direction to allow the phase matched THz generation in LiNbO₃ crystal.²⁰ The generated THz pulse energy after the crystal was measured by a commercial thermopile detector (Ophir 3A-P-THz), which was covered by a 4-mm-thick silicon wafer to block the scattered light from the pump beam. The THz output facet of the prism was anti-reflection coated by Kapton tape with a thickness of 60 µm to minimize the Fresnel loss. ²¹ The maximum THz pulse energy was 15 μ J under the infrared pump energy of 4.2 mJ before the LiNbO₃ crystal, corresponding to a pump-to-THz energy conversion efficiency of 0.35%. The THz pulse energy decreases with further increasing the pump intensity, which can be ascribed to the free carrier absorption of THz pulses in LiNbO₃. ^{18,22} The generated THz fields are vertically polarized. A pair of wire-grid THz polarizers was employed to attenuate the THz intensity as well as to change its polarization.

B. Tight focusing of THz beam

In THz nonlinear experiments, the field strength of the THz source determines its ability to interact nonlinearly with matters by driving them out of equilibrium state. Qualitatively, the THz

field strength is directly proportional to the square root of pulse energy but inversely proportional to the spot size. For the given pulse energy, the THz beam spot at focus should be as small as possible to achieve a higher field strength. Unfortunately, the long wavelengths associated with the THz frequency, 1 THz ~0.3 mm, and the multi-octave spanning frequency content make it difficult to tightly focus the THz beam. In principle, off-axis parabolic (OAP) mirrors with short focal length can be used to decrease the focused spot size. ^{23,24} However, this is even more difficult to implement with a 10 T split-pair magnet because only the OAP mirrors with focal lengths longer than 8 in. can be used due to the large size of the magnet, as shown in Fig. 1.

The generated THz beam was expanded by an OAP mirror telescope (OAP1 and OAP2) with a magnification factor of 10 and then focused into the center of the magnet by another OAP mirror (OAP3). Owing to the limited space between the magnet and its aluminum alloy mount, a third OAP mirror with 310 mm effective focal length and 3-in. diameter was employed, and its distance from the magnet center was fixed at 220 mm. To further decrease the focal spot size, the ray tracing method was employed to simulate and optimize the THz focusing optics. The wavelength for the investigation was 714 μ m, corresponding to 0.42 THz. After performing optimization, we found that an additional plane-convex high-density polyethylene (HDPE) lens (TL) with a focal length of 450 mm placed

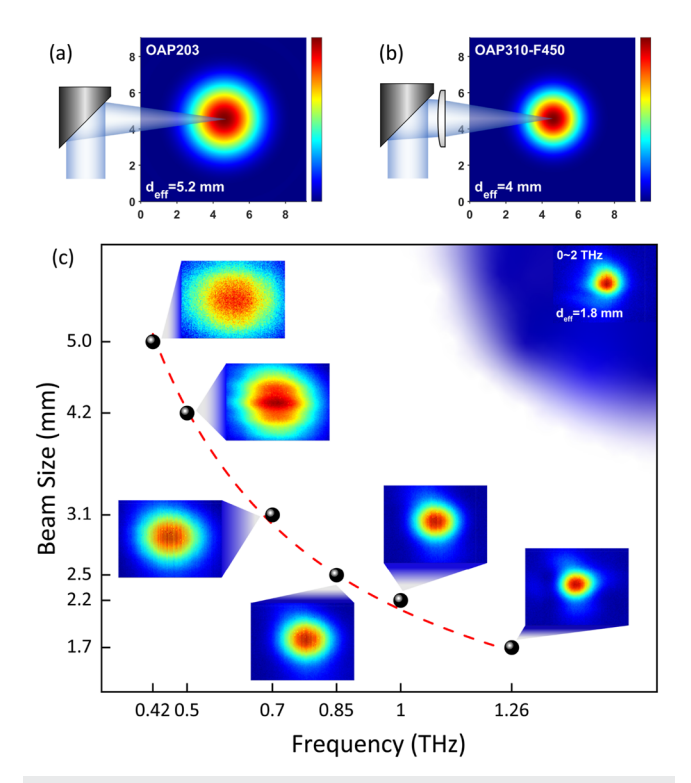


FIG. 2. Illustration of our ray tracing analysis performed in the optical design software for the THz focusing with (a) a single OAP mirror and (b) the combination of an OAP mirror and a HDPE lens. (c) The spot at the sample position measured with a THz camera for the multicycle THz pulses. The red dashed line is the fitting result using the inversely proportional formula. The inset shows the spot of the monocycle THz pulse.

TABLE I. Measured THz beam size and pulse energy at the sample position without and with two BPFs at different center frequencies.

Frequency (THz)	Beam size ^a (mm)	Pulse energy (μJ)
_b	1.8	9.5
0.42	5.0	0.54
0.5	4.2	0.85
0.7	3.1	0.74
0.85	2.5	0.58
1	2.2	0.58
1.26	1.7	0.11

 $^{^{}a)}1/e^2$ of power distribution.

directly after the OAP mirror (OAP3) can focus the THz beam right into the center of the superconducting magnet with a diameter of 4 mm, which is 22% smaller than the spot size of 5.2 mm focused by a single OAP mirror with a focal length of 203 mm, as illustrated in Figs. 2(a) and 2(b). This result indicates that the combination of an OAP mirror with a lens can be employed for tightly focusing the THz beam.

In order to demonstrate the feasibility of our approach, we measured the THz beam profile by using a commercial uncooled microbolometer camera (Swiss Terahertz S2×). The camera was placed at the sample position, i.e., the THz focal point, and the magnet was moved outside the optical path during the measurements. The THz intensity was attenuated by the polarizers to avoid the saturation of the camera. As illustrated in Fig. 2(c), the radially symmetric cross-section of the THz beam spot with a diameter of 1.8 mm $(1/e^2$ of power distribution) was realized by adopting the combination of the OAP mirror and HDPE lens. Moreover, the usage of an additional HDPE lens allows us to fine tune the THz focus position inside the magnet along the THz propagation direction.

To further characterize the THz beam around the focus, a set of bandpass filters (BPFs) with a bandwidth of 20% were inserted between the second and third OAP mirrors to produce the narrowband THz pump beam, as depicted in Fig. 1. We show the measured THz spot at the focus for different frequencies in Fig. 2(c). The image was fitted to a two-dimensional elliptical Gaussian function, where an effective diameter was obtained by the square mean of the major and minor axes of the fitted ellipse. As expected, the focused beam size decreases monotonically with increasing frequency. The extracted beam size and full THz pulse energy as a function of frequency at the sample position (without the magnet) are summarized in Table I. The THz pulse energy without the BPFs was 9.5 μ J, corresponding to an energy transfer efficiency of 63%. The relatively low value was caused by two factors: one is the THz beam misalignment in the long-distance propagation, and the other one is the absorption by water vapor in the THz pulse propagation in the atmosphere. Note that the THz beam path was not purged with nitrogen or dry air to remove the water vapor since there is no strong absorption at the frequencies of the BPFs used in our experiments.

C. Temporal and spectral THz pulse characteristics

After passing through the magnet, the THz beam was collimated and refocused on the detection crystal using a pair of 3 in.

diameter OAP mirrors (OAP4 and OAP5) with focal lengths of 7 and 2 in., respectively. The temporal profile of the terahertz electric field was measured by standard EO sampling with a 2-mm-thick ZnTe crystal. For the EO detection, two crossed THz polarizers were inserted to reduce the field intensity before the detection crystal. Figures 3(a) and 3(b) show the typical THz signals in the time and frequency domain, respectively. The monocycle THz pulses were centered around 0.8 THz and carried significant spectral intensity up to ~2 THz. Indeed, the majority of THz energy was concentrated at low frequencies below 1 THz, as listed in Table I. Figure 3 shows the multicycle THz electric field traces and corresponding spectra with two BPFs at different frequencies. The ratio of spectral bandwidth to nominal center frequency of multicycle THz pulses was less than 20%. It is noteworthy that the usage of non-magnetic holders and screws for OAP3 and OPA4, as well as the THz lens, can further eliminate the magnetic force experienced by the opto-mechanical components and hence guarantee a good THz phase stability even in high magnetic fields.

As the knowledge of THz field strength is crucial in THz non-linear experiments, we estimated the peak electric field in the THz beam focus by a combination of THz pulse energy ($\mathscr{E}_{\text{pulse}}$), beam size (d_{eff}), and EO sampling signal (E_{THz}) using the following equation:

$$\mathscr{E}_{\text{pulse}} = \frac{\pi}{8} \varepsilon_0 c d_{\text{eff}}^2 \int dt \ E_{\text{THz}}^2(t), \tag{1}$$

where ε_0 is the permittivity of vacuum and c is the speed of light. Using the parameters in Table I and the normalized waveform in Fig. 3(a), we obtained the peak electric field of 500 and several tens kV/cm for the monocycle and multicycle THz pulses, respectively. This method is widely used for characterization of intense THz, ^{19,25} even though it easily overestimates the actual field strength due to the multiple error factors about the measurement of the above-mentioned parameters.

D. Sample environment

Due to the use of optics with long focus length, we were able to integrate the intense THz source with a superconducting magnet (Oxford Spectromag SM4000). It was a split-pair, horizontal-field superconducting magnet system providing a sample environment with variable magnetic fields and low temperatures for optical measurements. The maximum magnetic field can go up to 10 T, and the sample temperature can be tuned by a variable temperature insert (VTI) in the range of 1.5-300 K. The windows of the VTI were upgraded to diamond, which features high transmission with spectral coverage from ultraviolet to terahertz, while z-cut quartz was used as the window of the outer vacuum chamber of the magnet for THz experiments. The magnet was mounted on a linear stage and a swing bearing, enabling convenient rotation of the magnetic field by 90° relative to the terahertz propagating direction (see supplementary material). Therefore, either the in-plane (Voigt configuration) or out-of-plane (Faraday configuration) magnetic field could be applied to the sample. Furthermore, a pair of PZT-driven linear and rotation stages (MultiFields Tech) were mounted at the end of the sample rod, as shown in Fig. 1(c). The linear stage allows us to move the sample up and down, and the rotation stage enables us to rotate the sample 360° about the sample surface. Both

b) Monocycle THz pulse without BPFs.

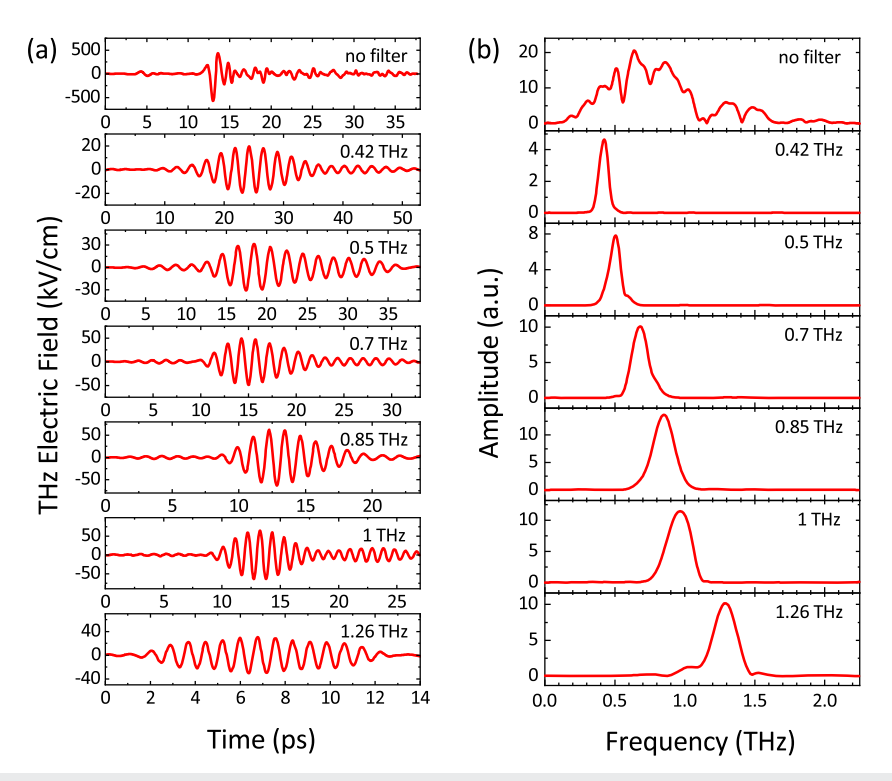


FIG. 3. (a) Measured temporal waveforms of the fundamental radiation electric field without and with THz BPFs, and (b) their corresponding Fourier-transformed spectra.

stages can work independently at temperatures as low as 1.5 K and magnetic fields up to $10~\mathrm{T}.$

III. INSTRUMENT PERFORMANCE

For demonstration of the performance of our instrument, we carried out studies of THz THG in a MgB2 thin film. High-quality single-crystalline MgB2 thin film with c-axis epitaxy and a thickness of 10 nm was grown on a MgO (111) substrate using a hybrid physical-chemical vapor deposition method. The film is known to have a T_c of 36 K. THz THG measurements have been reported previously in MgB_2 below T_c driven by intense narrowband THz In the following, we investigate the THG response of MgB2 as a function of temperature, sample azimuth angle, as well as in-plane and out-of-plane magnetic field. In the THz THG experiments, two BPFs with a center frequency of f = 0.42 THz were used to generate the narrowband pump pulses (see Fig. 3 for the time domain waveform and corresponding spectrum), and an additional 3f = 1.26 THz BPF was added after the sample to suppress the fundamental harmonic and extract the THG signal. The THz peak electric field of the fundamental THz beam was attenuated to 5 kV/cm.

Figure 4(a) displays the time trace of emitted radiation from MgB_2 at 2 K, which is clearly dominated by 3f oscillation. The Fourier transformed spectrum of the time-domain data, as shown in Fig. 4(b), exhibits a sharp peak at 1.26 THz and a negligible hump at 0.42 THz. As shown in Fig. 4(d), the THG intensity increases

with increasing temperature until it reaches a maximum around 26 K, after which it decreases rapidly and is dramatically reduced above T_c . This observation in MgB₂ is in agreement with earlier publications. The resonant behavior of THG intensity in the superconducting state has been ascribed to the resonant excitation of Higgs mode 3.28,29 when twice the pump frequency matches the superconducting gap frequency in the π band. The superconducting gap frequency in the π band.

It has been theoretically proposed that two competing scenarios,^{31–33} i.e., Higgs mode²³ and charge-density fluctuations,³⁴ both contribute to the nonlinear THG response but exhibit different dependence on the angle between the THz polarization and the crystal axis.³⁵ In previous experiments,^{26,35} two THz wire-grid polarizers were employed to rotate the incident THz polarization from vertical to horizontal, resulting in a reduction of the THz electric field by a factor of two. Additionally, two additional polarizers were placed behind the sample to correct the THz detection efficiency, which made the experiments complicated and introduced more uncertainty. Here, we can rotate the sample on site by 360° around the THz propagating direction. As shown in Fig. 4(c), the amplitude of the THG signal exhibits an isotropic response with respect to the rotation of the sample's azimuthal angle. This result indicates that the THG signal is independent of the pump polarization, which is similar to the previous results.²

To demonstrate the stability of our system, temperature-dependent THG measurements were performed with an external magnetic field applied both parallel (out-of-plane) and perpendicular (in-plane) to the c-axis of the sample. For the case of an

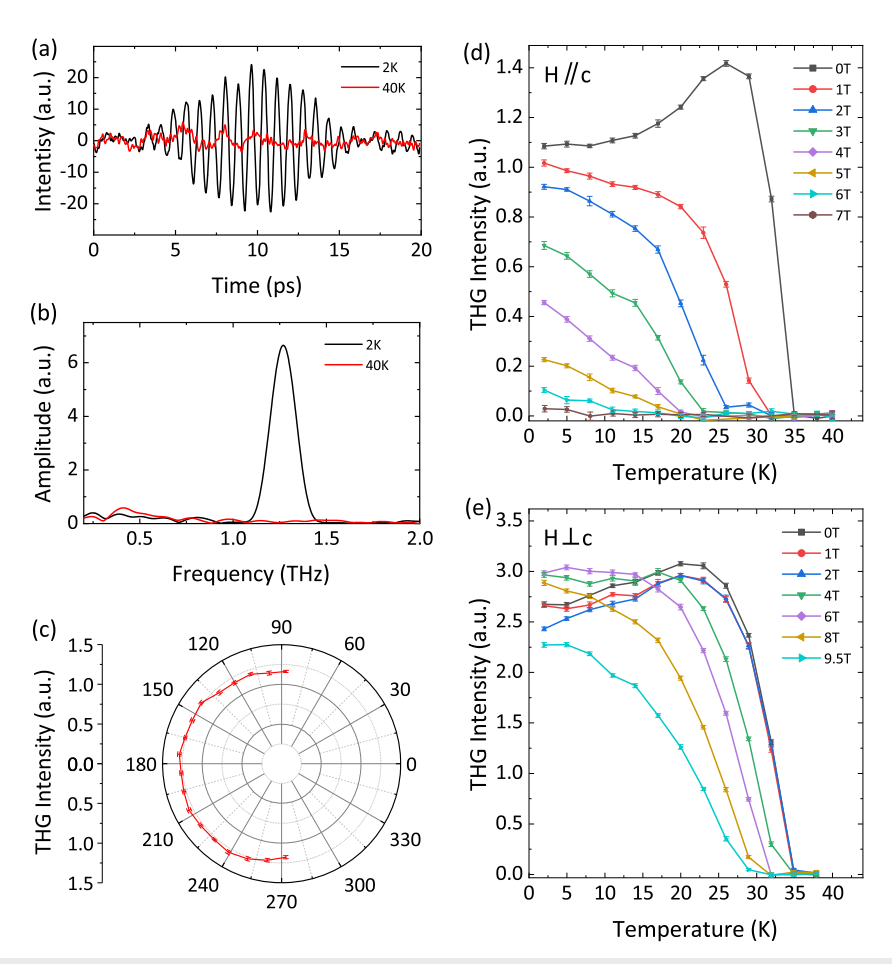


FIG. 4. THz THG results of MgB₂ film under the excitation of 0.42 THz pump pulses. (a) Temporal waveforms of the transmitted THz pulses at 2 and 40 K, respectively. A 1.26 THz BPF was inserted after the sample to suppress the transmitted fundamental component. (b) Fourier-transformed spectra of the corresponding time traces. (c) THG intensity as a function of sample azimuthal angle. Temperature dependence of the THG intensity measured in various magnetic fields, which were applied in both (d) out-of-plane and (e) in-plane directions to the film.

out-of-plane magnetic field, as presented in Fig. 4(d), the resonant peak disappears in finite fields. Instead, the THG intensity monotonically increases with decreasing temperature. Besides, the onset temperature of THG decreases with increasing magnetic field, and the THG signal roughly vanishes when the magnetic field is greater than 7 T. These observations are in line with the previous report.²⁷ Figure 4(e) shows the THG intensity vs temperature under in-plane magnetic fields up to 9.5 T. When the field is below 2 T, the THG intensity decreases slightly with a resonant feature around 20 K. The resonant peak shifts to 17 K at 4 T and disappears above 6 T. At low temperatures, the THG intensity increases slightly with increasing magnetic field from 2 to 6 T, then it is reduced with further increasing magnetic field. At higher temperatures, the THG intensity decreases monotonically with increasing magnetic field. At 9.5 T, the onset temperature of THG is around 30 K, and the THG amplitude at 2 K is comparable to that at zero field.

IV. DISCUSSION

The contrasting field-induced evolution of the THG responses for H $\parallel c$ and H \perp c can be ascribed to the anisotropic superconducting properties of MgB₂ under different magnetic fields. In the superconducting state, MgB₂ opens gaps on a two-dimensional σ -band and a three-dimensional π -band simultaneously, with values of $2\Delta_{\sigma}$ several times larger than $2\Delta_{\pi}$. $^{30,36-38}$ Such band structure leads to a highly anisotropic upper critical magnetic field in MgB₂. 39,40 The reported transport measurements reveal the upper critical field as $H_{c2}^{\perp} = 7.0 - 7.5$ T for H $\parallel c$, while for H \perp c the upper critical field H_{c2}^{\perp} extends up to above 20 T. 41 In the subsequent point-contact spectroscopy measurement, field dependences of the superconducting order parameters Δ_{π} and Δ_{σ} were measured with the field applied parallel and perpendicular to the film. 42 In the perpendicular field (H $\parallel c$), both order parameters collapse above H_{c2}^{\perp} . In the parallel

field (H \perp c), the Δ_{π} is completely suppressed when the field is larger than H_{c2}^{\parallel} , while the Δ_{σ} is decreasing much more gradually and survives to $H_{c2}^{\perp} \sim 20$ T. On the other hand, the typical two-gap feature of MgB2 leads to rich collective excitations of the superconducting order parameters. Besides the individual Higgs modes of Δ_{π} and Δ_{σ} order parameters, the coupling between the two order parameters introduces a massive phase mode, known as the Leggett mode, which locates between the two superconducting energy gaps $2\Delta_{\sigma}$ and $2\Delta_{\pi}$. At the current stage, which collective mode dominates the THz nonlinear signal is still under debate.⁴³ Our previous THz THG measurement suggests that the Higgs mode of Δ_{π} order parameter is the cause of the THG signal, ²⁶ while the single cycle THz pump-probe measurement indicates that the Leggett mode dominates the nonlinear response.⁴⁴ The dichromatic field dependences of the superconducting order parameters Δ_{π} and Δ_{σ} may provide an alternative route to distinguish the different contributions.

Figure 4(d) shows the magnetic field dependence of the THG signal with H $\|c$. Since the magnetic field kills the Δ_{π} and Δ_{σ} superconducting order parameters quickly for H $\parallel c$, the resonance temperature is suppressed to below the achieved lowest temperature (1.5 K) in our setup, leading to a monotonic increase of the THG intensity with decreasing temperature. When the magnetic field is rotated to in-plane (H \perp c), as shown in Fig. 4(e), the magnetic field evolution of the THG intensity is obviously distinct. As the magnetic field increases up to 6 T, the resonance peak shifts gradually toward lower temperature with a slight decrease in its intensity. Above 8 T, as described earlier, the Δ_{π} superconducting gap is closed, leading to the disappearance of the Δ_{π} Higgs mode and the Leggett mode. However, a sufficient THG signal survives above 8 T, which seems to be contradictory to the Δ_π Higgs mode predominated nonlinear response scenario. At 4 K with an in-plane 8 T magnetic field, the $\Delta_{\sigma}(8 \text{ T}, 4.2 \text{ K})$ is roughly 5 meV according to the previous point-contact spectroscopy measurement.⁴² If the residual THG signal above 8 T is contributed by Δ_{σ} Higgs mode, a resonance behavior should be observed in the vicinity of temperatures where the resonance condition would be fulfilled for the gap in the σ -band. The absence of resonance behavior suggests that further THz pump-probe measurement under in-plane magnetic fields is desirable to identify the intrinsic frequency of the superconducting order parameter above 8 T and eventually elucidate the different contributions.

V. CONCLUSIONS

In this work, we report the combination of the laser-driven table-top strong-field THz source with a superconducting magnet to achieve the measurement of THz nonlinear spectroscopy at low temperatures and under high magnetic fields. The intense THz pump beam was generated from LiNbO₃ crystal by using the tilted-pulse-front technique and tightly focused into the center of the magnet by an off-axis parabolic mirror and a THz lens. We demonstrate the excellent performance of our instrument by conducting the THG measurements in the two-band superconductor MgB₂ with a superconducting transition temperature of 36 K as a function of temperature, sample azimuth angle, as well as in-plane and out-of-plane magnetic field. This state-of-the-art instrument will enable us to study a variety of materials with magnetic field

dependent properties of interest, such as correlated electronic materials like superconductors, transition metal oxides, and topological materials.

SUPPLEMENTARY MATERIAL

See the supplementary material for the illustration video of the rotation of the magnetic field.

ACKNOWLEDGMENTS

This work was supported by the National Natural Science Foundation of China (Grant Nos. 11974414, 12488201, 92365102, and 12134018) and the National Key Research and Development Program of China (Grant Nos. 2021YFA1400200, 2022YFA1403901, and 2022YFA1602800). This work was carried out at the infrared and terahertz spectra measurement station of the Synergetic Extreme Condition User Facility (SECUF).

AUTHOR DECLARATIONS

Conflict of Interest

The authors have no conflicts to disclose.

Author Contributions

X.B. Wang and H.W contributed equally to this work.

X. B. Wang: Funding acquisition (equal); Methodology (equal); Supervision (equal); Writing – original draft (equal); Writing – review & editing (equal). H. Wang: Methodology (equal); Writing – original draft (equal). J. Y. Yuan: Methodology (supporting). X. Y. Zeng: Methodology (supporting). L. Cheng: Methodology (supporting). J. Qi: Funding acquisition (supporting); Methodology (supporting). J. L. Luo: Funding acquisition (equal); Methodology (supporting). T. Dong: Funding acquisition (equal); Methodology (equal); Supervision (equal); Writing – original draft (equal); Writing – review & editing (equal). N. L. Wang: Funding acquisition (equal); Methodology (supporting); Supervision (equal); Writing – review & editing (equal).

DATA AVAILABILITY

The data that support the findings of this study are available from the corresponding author upon reasonable request.

REFERENCES

¹D. N. Basov, R. D. Averitt, D. van der Marel, M. Dressel, and K. Haule, Rev. Mod. Phys. 83, 471 (2011).

²Z. Wang, S. Reschke, D. Hüvonen, S.-H. Do, K.-Y. Choi, M. Gensch, U. Nagel, T. Rō om, and A. Loidl, Phys. Rev. Lett. **119**, 227202 (2017).

³Z. Wang, J. Wu, W. Yang, A. K. Bera, D. Kamenskyi, A. Islam, S. Xu, J. M. Law, B. Lake, C. Wu, and A. Loidl, Nature 554, 219 (2018).

⁴L. Y. Shi, Y. Q. Liu, T. Lin, M. Y. Zhang, S. J. Zhang, L. Wang, Y. G. Shi, T. Dong, and N. L. Wang, Phys. Rev. B **98**, 094414 (2018).

- ⁵L. Y. Shi, X. M. Wang, R. D. Zhong, Z. X. Wang, T. C. Hu, S. J. Zhang, Q. M. Liu, T. Dong, F. Wang, and N. L. Wang, Phys. Rev. B **104**, 144408 (2021).
- ⁶R. Shimano, G. Yumoto, J. Y. Yoo, R. Matsunaga, S. Tanabe, H. Hibino, T. Morimoto, and H. Aoki, Nat. Commun. 4, 1841 (2013).
- ⁷V. Dziom, A. Shuvaev, A. Pimenov, G. V. Astakhov, C. Ames, K. Bendias, J. Bottcher, G. Tkachov, E. M. Hankiewicz, C. Brune, H. Buhmann, and L. W. Molenkamp, Nat. Commun. 8, 15197 (2017).
- ⁸L. Wu, M. Salehi, N. Koirala, J. Moon, S. Oh, and N. P. Armitage, Science 354, 1124 (2016).
- ⁹M. L. Sadowski, G. Martinez, M. Potemski, C. Berger, and W. A. de Heer, Phys. Rev. Lett. **97**, 266405 (2006).
- ¹⁰ Z. Jiang, E. A. Henriksen, L. C. Tung, Y.-J. Wang, M. E. Schwartz, M. Y. Han, P. Kim, and H. L. Stormer, Phys. Rev. Lett. **98**, 197403 (2007).
- ¹¹T. Maag, A. Bayer, S. Baierl, M. Hohenleutner, T. Korn, C. Schüller, D. Schuh, D. Bougeard, C. Lange, R. Huber, M. Mootz, J. E. Sipe, S. Koch, and M. Kira, Nat. Phys. 12, 119 (2016).
- ¹²G. Yumoto, R. Matsunaga, H. Hibino, and R. Shimano, Phys. Rev. Lett. 120, 107401 (2018).
- ¹³P. Gogoi, D. Kamenskyi, D. D. Arslanov, R. T. Jongma, W. J. van der Zande, B. Redlich, A. F. G. van der Meer, H. Engelkamp, P. C. M. Christianen, and J. C. Maan, Phys. Rev. Lett. 119, 146603 (2017).
- ¹⁴J. C. König-Otto, Y. Wang, A. Belyanin, C. Berger, W. A. de Heer, M. Orlita, A. Pashkin, H. Schneider, M. Helm, and S. Winnerl, Nano Lett. 17, 2184 (2017).
- ¹⁵M. Mittendorff, F. Wendler, E. Malic, A. Knorr, M. Orlita, M. Potemski, C. Berger, W. A. de Heer, H. Schneider, M. Helm, and S. Winnerl, Nat. Phys. 11, 75 (2015).
- ¹⁶H. Chu, S. Kovalev, Z. X. Wang, L. Schwarz, T. Dong, L. Feng, R. Haenel, M.-J. Kim, P. Shabestari, L. P. Hoang, K. Honasoge, R. D. Dawson, D. Putzky, G. Kim, M. Puviani, M. Chen, N. Awari, A. N. Ponomaryov, I. Ilyakov, M. Bluschke, F. Boschini, M. Zonno, S. Zhdanovich, M. Na, G. Christiani, G. Logvenov, D. J. Jones, A. Damascelli, M. Minola, B. Keimer, D. Manske, N. Wang, J.-C. Deinert, and S. Kaiser, Nat. Commun. 14, 1343 (2023).
- 17 J. Hebling, G. Almási, I. Z. Kozma, and J. Kuhl, Opt. Express 10, 1161 (2002).
- ¹⁸J. A. Fülöp, L. Pálfalvi, G. Almási, and J. Hebling, Opt. Express 18, 12311 (2010).
- ¹⁹F. Blanchard, G. Sharma, L. Razzari, X. Ropagnol, H.-C. Bandulet, F. Vidal, R. Morandotti, J.-C. Kieffer, T. Ozaki, H. Tiedje, H. Haugen, M. Reid, and F. Hegmann, IEEE J. Sel. Top. Quantum Electron. 17, 5 (2011).
- ²⁰H. Hirori, A. Doi, F. Blanchard, and K. Tanaka, Appl. Phys. Lett. **98**, 091106 (2011).
- ²¹B. Zhang, Z. Ma, J. Ma, X. Wu, C. Ouyang, D. Kong, T. Hong, X. Wang, P. Yang, L. Chen, Y. Li, and J. Zhang, Laser Photonics Rev. 15, 2000295 (2021).
- ²²J. A. Fülöp, L. Pálfalvi, S. Klingebiel, G. Almási, F. Krausz, S. Karsch, and J. Hebling, Opt. Lett. **37**, 557 (2012).

- ²³ R. Matsunaga, N. Tsuji, H. Fujita, A. Sugioka, K. Makise, Y. Uzawa, H. Terai, Z. Wang, H. Aoki, and R. Shimano, Science 345, 1145 (2014).
- ²⁴B. Cheng, N. Kanda, T. N. Ikeda, T. Matsuda, P. Xia, T. Schumann, S. Stemmer, J. Itatani, N. P. Armitage, and R. Matsunaga, Phys. Rev. Lett. 124, 117402 (2020).
- ²⁵M. Sajadi, M. Wolf, and T. Kampfrath, "Terahertz-field-induced optical bire-fringence in common window and substrate materials," Opt. Express 23, 28985 (2015).
- ²⁶S. Kovalev, T. Dong, L.-Y. Shi, C. Reinhoffer, T.-Q. Xu, H.-Z. Wang, Y. Wang, Z.-Z. Gan, S. Germanskiy, J.-C. Deinert, I. Ilyakov, P. H. M. van Loosdrecht, D. Wu, N.-L. Wang, J. Demsar, and Z. Wang, Phys. Rev. B 104, L140505 (2021).
- ²⁷C. Reinhoffer, P. Pilch, A. Reinold, P. Derendorf, S. Kovalev, J.-C. Deinert, I. Ilyakov, A. Ponomaryov, M. Chen, T.-Q. Xu, Y. Wang, Z.-Z. Gan, D.-S. Wu, J.-L. Luo, S. Germanskiy, E. A. Mashkovich, P. H. M. van Loosdrecht, I. M. Eremin, and Z. Wang, Phys. Rev. B 106, 214514 (2022).
- ²⁸R. Shimano and N. Tsuji, Annu. Rev. Condens. Matter Phys. 11, 103 (2020).
- ²⁹ N. Tsuji and H. Aoki, *Phys. Rev. B* **92**, 064508 (2015).
- ³⁰ M. Iavarone, G. Karapetrov, A. E. Koshelev, W. K. Kwok, G. W. Crabtree, D. G. Hinks, W. N. Kang, E.-M. Choi, H. J. Kim, H.-J. Kim, and S. I. Lee, Phys. Rev. Lett. 89, 187002 (2002).
- ³¹ L. Schwarz and D. Manske, Phys. Rev. B 101, 184519 (2020).
- ³²N. Tsuji, Y. Murakami, and H. Aoki, *Phys. Rev. B* **94**, 224519 (2016).
- ³³ R. Haenel, P. Froese, D. Manske, and L. Schwarz, Phys. Rev. B **104**, 134504 (2021).
- 34T. Cea, C. Castellani, and L. Benfatto, Phys. Rev. B 93, 180507 (2016).
- ³⁵R. Matsunaga, N. Tsuji, K. Makise, H. Terai, H. Aoki, and R. Shimano, Phys. Rev. B 96, 020505 (2017).
- ³⁶ J. Kortus, I. I. Mazin, K. D. Belashchenko, V. P. Antropov, and L. L. Boyer, Phys. Rev. Lett. **86**, 4656 (2001).
- ³⁷ A. D. Caplin, Y. Bugoslavsky, L. F. Cohen, L. Cowey, J. Driscoll, J. Moore, and G. K. Perkins, Supercond. Sci. Technol. 16, 176 (2002).
- ³⁸ P. Szabó, P. Samuely, J. Kačmarčík, T. Klein, J. Marcus, D. Fruchart, S. Miraglia, C. Marcenat, and A. G. M. Jansen, Phys. Rev. Lett. 87, 137005 (2001).
- ³⁹L. Lyard, P. Samuely, P. Szabo, T. Klein, C. Marcenat, L. Paulius, K. H. P. Kim, C. U. Jung, H.-S. Lee, B. Kang, S. Choi, S.-I. Lee, J. Marcus, S. Blanchard, A. G. M. Jansen, U. Welp, G. Karapetrov, and W. K. Kwok, Phys. Rev. B 66, 180502 (2002).
- ⁴⁰U. Welp, A. Rydh, G. Karapetrov, W. K. Kwok, G. W. Crabtree, C. Marcenat, L. M. Paulius, L. Lyard, T. Klein, J. Marcus, S. Blanchard, P. Samuely, P. Szabo, A. G. M. Jansen, K. H. P. Kim, C. U. Jung, H. S. Lee, B. Kang, and S. I. Lee, Physica C 385, 154 (2003).
- ⁴¹Y. Eltsev, S. Lee, K. Nakao, N. Chikumoto, S. Tajima, N. Koshizuka, and M. Murakami, Phys. Rev. B 65, 140501 (2002).
- ⁴²Y. Bugoslavsky, Y. Miyoshi, G. K. Perkins, A. D. Caplin, L. F. Cohen, A. V. Pogrebnyakov, and X. X. Xi, Phys. Rev. B 69, 132508 (2004).
- ⁴³T. Dong, S.-J. Zhang, and N.-L. Wang, Adv. Mater. **35**, 2110068 (2023).
- ⁴⁴F. Giorgianni, T. Cea, C. Vicario, C. P. Hauri, W. K. Withanage, X. Xi, and L. Benfatto, Nat. Phys. 15, 341 (2019).